Searching for Dark Matter with a Superconducting Qubit

Supplementary Information

Akash V. Dixit,[1,2,3,*] Srivatsan Chakram,[1,2,4] Kevin He,[1,2] Ankur Agrawal,[1,2,3] Ravi K. Naik,[5] David I. Schuster,[1,2,6] and Aaron Chou[7]

[1] *James Franck Institute, University of Chicago, Chicago, Illinois 60637, USA*
[2] *Department of Physics, University of Chicago, Chicago, Illinois 60637, USA*
[3] *Kavli Institute for Cosmological Physics, University of Chicago, Chicago, Illinois 60637, USA*
[4] *Department of Physics and Astronomy, Rutgers University, Piscataway, New Jersey 08854, USA*
[5] *Department of Physics, University of California Berkeley, California 94720, USA*
[6] *Pritzker School of Molecular Engineering, University of Chicago, Chicago, Illinois 60637, USA*
[7] *Fermi National Accelerator Laboratory, Batavia, Illinois 60510, USA*

Dark matter induced signal

We use the potential interaction of the dark matter with electromagnetism as the basis for a search protocol. The dark matter candidate forms an effective oscillating current density that sources Maxwell's equations. Via Faraday's law, the electric field of a microwave cavity is sourced by the effective current formed by the dark matter $\nabla \times \mathbf{B} - \frac{\partial \mathbf{E}}{\partial t} = \mathbf{j}_{\mathrm{DM}}$. For axions, the effective current density is $\mathbf{j}_{\mathrm{axion}} = g_{a\gamma\gamma}\sqrt{2\rho}\mathbf{B}_0 e^{im_a t}$, where $g_{a\gamma\gamma}$ is the predicted coupling of the axion field to electromagnetism, ρ is the local dark matter density, $\mathbf{B}_0$ is a DC magnetic field applied in the laboratory, and m_a is the mass of the axion. For hidden photons, the effective current is $\mathbf{j}_{\mathrm{HP}} = \epsilon m_{\gamma'}\sqrt{2\rho}e^{im_{\gamma'}t}\hat{\mathbf{u}}$, where ϵ is a postulated kinetic angle of mixing between standard electromagnetism and hidden sector electromagnetism, $\hat{\mathbf{u}}$ is the polarization of the hidden photon field, and $m_{\gamma'}$ is the hidden photon mass. A microwave cavity tuned to the hypothetical mass of the dark matter candidate is used to accumulate the signal before it is read out.

Flute cavity fabrication

The cavities used in this work are fabricated from high purity (99.9999%) Aluminium using a novel flute method illustrated in Fig. S1. This technique involves drilling offset holes from the top and bottom of the stock material, with a region of overlap defining the cavity volume. Making the cavity from a monolithic piece of Aluminium eliminates seam loss by design [1] and results in a high quality factor. The full device consists of two microwave cavities each coupled to the transmon qubit. One cavity has a long lived storage mode and the other is strongly coupled to the line to perform qubit readout.

Transmon qubit fabrication

The transmon qubits were fabricated on 430 µm thick C-plane (0001) Sapphire wafers with a diameter of 50.8 mm. Wafers were cleaned with organic solvents (Toluene, Acetone, Methanol, Isopropanol, and DI water) in an ultrasonic bath to remove contamination, then were annealed at 1200 °C for 1.5 hours. Prior to film deposition, wafers underwent a second clean with organic solvents (Toluene, Acetone, Methanol, Isopropanol, and DI water) in an ultrasonic bath. The base layer of the device, which includes the capacitor pads for the transmon, consists of 75 nm of Nb deposited via electron-beam evaporation at 1 Å/s. The features were defined via optical lithography using AZ MiR 703 photoresist, and exposure with a Heidleberg MLA150 Direct Writer. The resist was developed for 1 minute in AZ MIF 300 1:1. The features were etched in a Plasma-Therm inductively coupled plasma (ICP) etcher using fluorine based ICP etch chemistry with a plasma consisting of 15 sccm SF_6, 40 sccm CHF_3, and 10 sccm Ar. The junction mask was defined via electron-beam lithography of a bi-layer resist (MMA-PMMA) in the Manhattan pattern using a Raith EBPG5000 Plus E-Beam Writer, with overlap pads for direct galvanic contact to the optically defined capacitors. The resist stack was developed for 1.5 minutes in a solution of 3 parts IPA

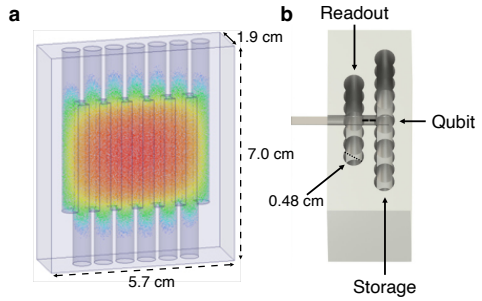

FIG. S1. **Illustration of the device. a,** A monolithic rectangular flute cavity composed entirely of blind evanescent holes with diameter equal to the width of the cavity, drilled from both the top and bottom of the stock. The depth of the evanescent holes is chosen so the exponentially decaying field results in quality factors $> 10^9$. The electric field ($|\mathbf{E}|$) of its fundamental mode is plotted on a logarithmic scale. **b,** Rendering of half of the device including storage cavity, readout cavity, and transmon qubit.

and 1 part DI water. Before deposition, the overlap regions on the pre-deposited capacitors were milled *in-situ* with an Argon ion mill to remove the native oxide. The junctions were then deposited with a three step electron-beam evaporation and oxidation process. First, an initial 35 nm layer of aluminium was deposited at 1 nm/s at an angle of 29° relative to the normal of the substrate, parallel azimuthally to one of the fingers in the Manhattan pattern for each of the junctions. Next, the junctions were exposed to 20 mbar of a high-purity mixture of Ar and O_2 (ratio of 80:20) for 12 minutes for the first layer to grow a native oxide. Finally, a second 120 nm layer of aluminium was deposited at 1 nm/s at the same angle relative to the normal of the substrate, but orthogonal azimuthally to the first layer of aluminium. After evaporation, the remaining resist was removed via liftoff in N-Methyl-2-pyrrolidone (NMP) at 80 °C for 3 hours, leaving only the junctions directly connected to the base layer. After both the evaporation and liftoff, the device was exposed to an ion-producing fan for 15 minutes, in order to avoid electrostatic discharge of the junctions. The room temperature DC resistance of the Josephson junction on each qubit was measured to select the qubit which corresponds to the target Josephson energy [2] (E_J).

Experimental setup

The cavities and qubit are mounted to the base plate of a dilution fridge (Bluefors LD400) operating at 8 mK. The device is potted in a block of infrared (IR) absorbant material (eccosorb CR-110) to absorb stray radiation and housed in two layers of μ-metal to shield from magnetic fields. Signals sent to the device are attenuated and thermalized at each temperature stage of the cryostat as shown in Fig. S2. The field probing the readout resonator is injected via the weakly coupled port (shorter dipole stub antenna). Control pulses for qubit, storage cavity, and sideband operation are inserted through the strongly coupled readout port (longer dipole stub antenna). This line includes a cryogenic microwave attenuator thermalized to the base stage (Courtesy of B. Palmer) and a weak eccosorb (IR filter). Both control lines also contain an inline copper coated XMA attenuator that is threaded to the base state. The signal from the readout resonator reflects off a Josephson parametric amplifier (not used in this work) before being amplified by a cryogenic HEMT amplifier at the 4 K stage. The output is mixed down to DC before being digitized.

Calibration of parity measurement

The cavity number parity measurement requires the calibration of the two qubit $\pi/2$ pulses as well as the delay between them. To set the $\pi/2$ pulse length, we perform qubit Rabi oscillations between the $|g\rangle$ and $|e\rangle$ levels by driving at the qubit transition frequency. The population

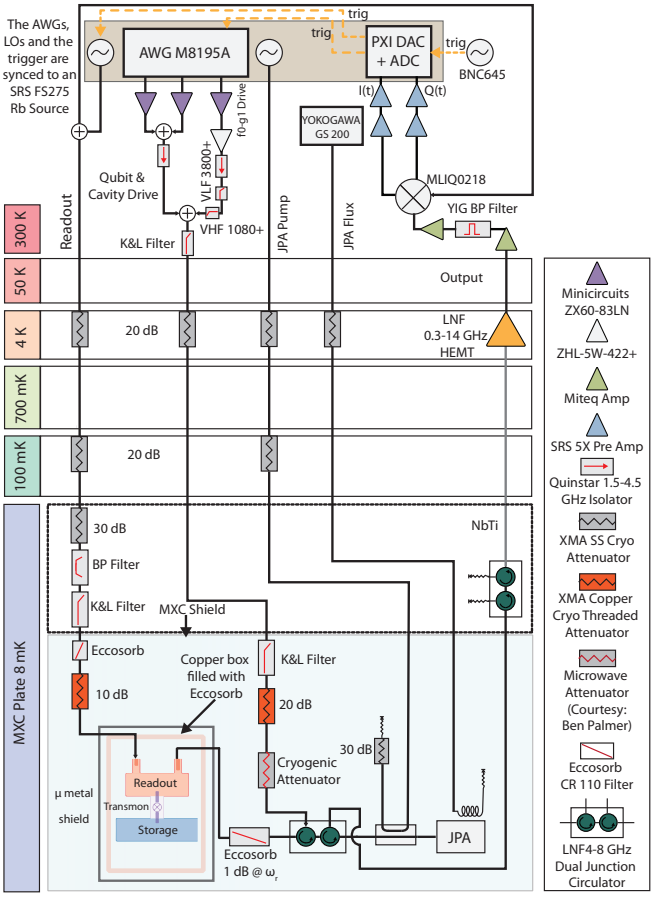

FIG. S2. **Wiring diagram inside the dilution refrigerator and the room temperature measurement setup.** Qubit readout is performed by injecting a drive into the weakly coupled port. After interacting with the readout cavity, the signal is routed to the amplification chain using non reciprocal circulator and isolator elements. We note, the Josephson parametric amplifier is not in operation for the measurements presented in this work. The signal is then mixed down to DC, further amplified, and finally digitized. Qubit and storage cavity operations are performed via the strongly coupled port. This line is heavily filtered and attenuated [3] to minimize stray radiation from entering the device.

transfer is sinusoidal and can be fit to determine when the qubit population has inverted (π pulse). By turning on the drive for only half the time required to perform a π pulse gives us the needed $\pi/2$ pulse to put the qubit in a clock state ($\frac{1}{\sqrt{2}}(|g\rangle + |e\rangle)$). The parity measurement is comprised of an initial $\pi/2$ pulse followed by a time delay of $\pi/|2\chi|$ and a final $-\pi/2$ pulse (constructed by advancing the phase of the $\pi/2$ pulse by π).

To calibrate the time delay used in the parity measurement, we perform two Ramsey interferometry experiments on the qubit either in the absence or presence of a single photon in the cavity. We chose the Ramsey drive frequency to be on resonance with the qubit transition

frequency. In the absence of the photon, the qubit superposition remains unchanged in the frame of the qubit. We use the $|f0\rangle - |g1\rangle$ sideband [4–7] to populate the cavity with a single photon. In the presence of the cavity photon, the qubit transition frequency is shifted by 2χ relative to the Ramsey frequency, consequently, the resulting fringe oscillates at a rate of 2χ. The parity measurement delay time (t_p) is chosen such that the qubit superposition state has obtained a phase shift of π. This is also a calibration of the dispersive shift ($|2\chi| = \pi/t_p$).

Drive pulse calibration

By applying a weak coherent tone at the storage cavity frequency, we induce a variable displacement α of the cavity state. We calibrate the number of photons injected into the storage cavity by varying the drive amplitude and performing qubit spectroscopy. By fitting the qubit spectrum show in Fig. S3 to a Poisson distribution, we extract the cavity occupation, $\bar{n} = |\alpha|^2$.

Nonlinearities of the signal generator result in a non trivial relationship between drive amplitude (at the software level) and the cavity occupation number. We map the transfer function that describes this relation and use it to apply calibrated cavity displacements (Fig. S4).

Elements of hidden Markov model

The hidden Markov model relies on independent measurements of the probabilities contained in the transition and emission matrices. The elements of these matricies depend on the parameters of the experiment and the device, including the lifetimes of the qubit and cavity, qubit spurious population, and readout fidelities.

Transmission matrix elements

The lifetime of the qubit is determined by applying a π pulse and waiting for a variable time before measuring the population. We map out the qubit population as a function of the delay time, fit it with an exponential characterizing the Poissonian nature of the decay process, and obtain $T_1^q = 108 \pm 18\,\mu s$.

The dephasing time of the qubit is measured by a Ramsey interferometry experiment with a $\pi/2$ pulse, variable delay, and a final $\pi/2$ with its phase advanced by $\omega_r t$ where ω_r is the Ramsey frequency. During the variable delay period, a series of π pulses are applied to perform spin echos and reduce sensitivity to low frequency noise. We observe a dephasing time of $T_2^q = 61 \pm 4\,\mu s$.

The storage cavity lifetime is calibrated by performing a cavity T_1 experiment. This is accomplished by applying a π_{ge} pulse and a π_{ef} to the transmon. This is followed by driving the $|f0\rangle - |g1\rangle$ transition, mediated by the Josephson nonliniearity for a time corresponding to a π pulse [4–7]. This populates the cavity with $|n\rangle = |1\rangle$ photons. After a variable time delay, the cavity population is swapped back into the qubit using the same $\pi_{|f0\rangle-|g1\rangle}$ pulse. Measuring the qubit population, we infer the cavity population as a function of the time delay. This is fit with a decaying exponential to obtain $T_1^s = 546 \pm 23\,\mu s$ (Fig. S5). To measure the cavity dephasing time, the cavity is initialized in a superposition state $\frac{1}{\sqrt{2}}(|0\rangle + |1\rangle)$ by first applying a $\pi_{ge}/2$ pulse, a π_{ef}, followed by a $\pi_{|f0\rangle-|g1\rangle}$ pulse. A Ramsey measurement is performed to obtain a cavity dephasing time of $T_2^s = 774 \pm 286\,\mu s$.

The qubit spurious population is determined by measuring the relative populations of its ground and excited states [8]. This is done by utilizing the f-level of the transmon. Two Rabi experiments are conducted swapping population between the $|e\rangle$ and $|f\rangle$ levels. First, we apply a π_{ge} pulse to invert the qubit population followed by the $|e\rangle - |f\rangle$ Rabi experiment. Second, no π_{ge} pulse is

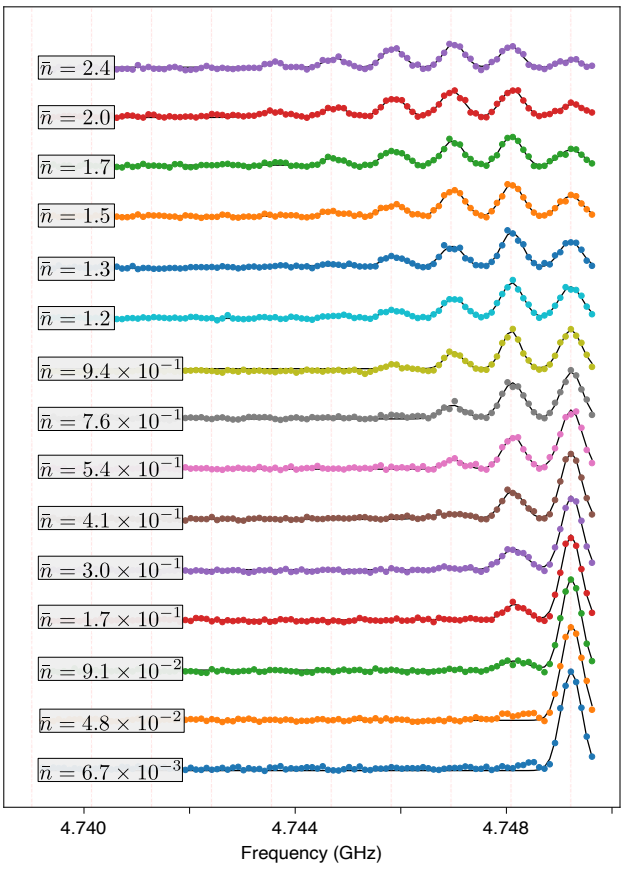

FIG. S3. **Qubit spectroscopy reveals cavity displacement** The cavity is displaced using a variable weak coherent drive for a finite period of time. The resulting population of the cavity is determined by performing qubit spectroscopy (points). The cavity photon number dependent shift of the qubit transition frequency reveals the cavity population. By fitting to the spectrum (black) we extract the weights of the cavity number states in the prepared coherent state.

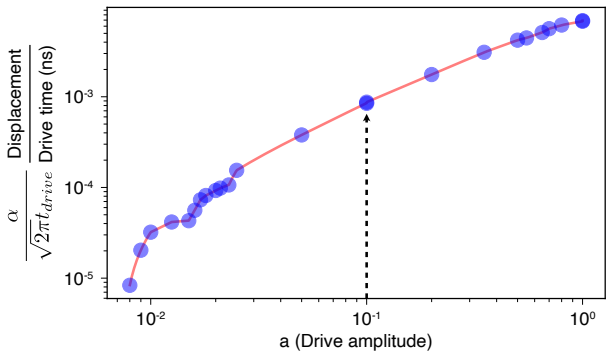

FIG. S4. **Transfer function describing mapping between drive amplitude in software and cavity displacement.** This transfer function is calibrated such that the cavity is displaced by α when we use a coherent drive of length t_{drive} and amplitude of a (in software) at the cavity frequency. Blue points are obtained by fitting to qubit spectroscopy after applying cavity displacements with variable drive time. For example, a 10ns pulse with a = 0.1 (indicated by the arrow) produces a cavity displacement of $\alpha = 2.1 \times 10^{-1}$. The red curve is a linear interpolation between the data points and can be used to generate displacements that are not directly calibrated. The data points are chosen to capture the nonlinear behavior of the waveform generator at values where an additional bit is necessary to represent the drive amplitude.

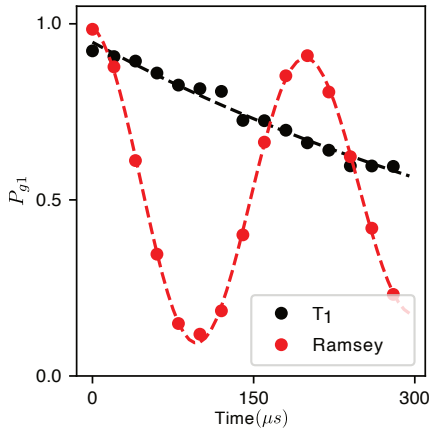

FIG. S5. **Storage cavity lifetime and dephasing time from T_1 and Ramsey measurements.** The long lived storage cavity mode is ideal for holding a signal photon induced by the dark matter while a series of repeated photon counting measurements is performed.

applied before the ef Rabi oscillation. The ratio of the amplitudes of the oscillations gives us the ratio of the populations of the excited and ground state. Assuming that $P(g) + P(e) = 1$ and measuring $\frac{P(e)}{P(g)}$, we obtain $P(g) = 0.949$ and $P(e) = 0.051$, corresponding to an effective qubit temperature of 71 mK.

Emission matrix elements

In order to characterize the emission matrix it is necessary to measure the readout infidelity of a particular transmon state. All the possible transmon states ($|g\rangle, |e\rangle, |f\rangle$) are prepared (3000 independent experiments per state) and the resulting I,Q signals are digitized. The resulting distributions in I,Q space are used as a map to determine the probability that any readout signal is the result of transmon being in either $|g\rangle, |e\rangle$, or $|f\rangle$. Based on the calculated probability, the state is assigned to either $\mathcal{G}, \mathcal{E}$, or $\mathcal{F}$ (Fig. S6).

Readout errors are due to voltage excursions from amplifier noise or spurious qubit transitions. The emission matrix should only contain readout errors that occur due to voltage fluctuations. Errors due to qubit transitions during the readout window are accounted for in the transition matrix. To disentangle the two contributions the analysis is run with various contingencies, all resulting in the same detector false positive probability and efficiency, indicating that the Markov model is robust to small perturbations of the emission matrix when so heavily biased against false positives. In the most conservative case, the qubit errors are accounted for during the entire 10 µs window or each parity measurement. The readout infidelity is determined by finding how many errors are made (regardless of the source) during the 3 µs readout window (part of the 10 µs experiment time window). In this case qubit errors are counted twice during the readout window. In the second case, we consider qubit errors only for times when readout is not occurring (7 of the 10 µs) and include all error channels in the readout infidelity. This avoids double counting of the qubit error during readout. The third case most closely aligns with the plausible physical model of errors during the readout window occurring due to a combination of qubit errors and amplifier noise. The readout infidelity is computed by subtracting the qubit error probabilities during the 3 µs readout window due to qubit decay ($1 - e^{-3\,\mu s/T_1^q}$) or heating ($\bar{n}_q[1 - e^{-3\,\mu s/T_1^q}]$) from the total measured error during readout, leaving only readout errors due to voltage noise from amplifiers. This is the readout infidelity used to determine the elements of the emission matrix in the analysis.

Detector characterization

To characterize the detector, the cavity population is varied by applying a weak drive and the cavity photon number is counted using the technique described in the main text. In order to extract the efficiency (η) and false positive probability (δ) of the detector, the relationship between injected photon population ($\bar{n}_{\rm inj}$) and measured photon population ($\bar{n}_{\rm meas}$) is fit to $\bar{n}_{\rm inj} = \eta \times \bar{n}_{\rm meas} + \delta$.

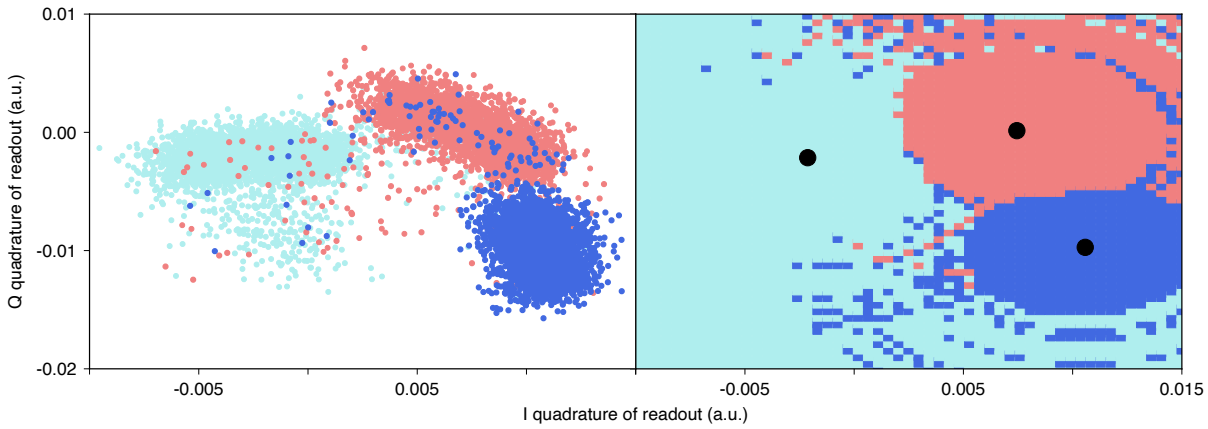

FIG. S6. **Mapping of readout measurements to transmon states.** (Left) Transmon is prepared in one of its possible states ($|g\rangle, |e\rangle, |f\rangle$ in blue, red, cyan) 3000 times each and the corresponding readout signals are recorded. (Right) From the readout data we can generate a map that takes a new measurement (point in IQ space) and returns a readout signal, $\mathcal{G}, \mathcal{E}$, or $\mathcal{F}$. All measurements that fall outside of the subspace of $|g\rangle$ and $|e\rangle$ are assigned to $|f\rangle$ since the parity measurement only makes use of the first two levels of the transmon.

Device Parameter	Value
Qubit frequency	$\omega_q = 2\pi \times 4.749\,\text{GHz}$
Qubit anharmonicity	$\alpha_q = -139.5\,\text{MHz}$
Qubit decay time	$T_1^q = 108 \pm 18\,\mu\text{s}$
Qubit dephasing time	$T_2^q = 61 \pm 4\,\mu\text{s}$
Qubit residual occupation	$\bar{n}_q = 5.1 \pm 0.3 \times 10^{-2}$
Storage frequency	$\omega_s = 2\pi \times 6.011\,\text{GHz}$
Storage decay time	$T_1^s = 546 \pm 23\,\mu\text{s}$
Storage dephasing time	$T_2^s = 774 \pm 286\,\mu\text{s}$
Storage-Qubit Stark shift	$2\chi = -2\pi \times 1.13\,\text{MHz}$
Storage residual occupation	$\bar{n}_q = 7.3 \pm 2.9 \times 10^{-4}$
Readout frequency	$\omega_r = 2\pi \times 8.052\,\text{GHz}$
Readout $\|e\rangle$ shift	$2\chi_r^e = -2\pi \times 0.38\,\text{MHz}$
Readout $\|f\rangle$ shift	$2\chi_r^f = -2\pi \times 0.73\,\text{MHz}$
Readout fidelity ($\|g\rangle$)	$F_{g\mathcal{G}} = 95.8 \pm 0.4\,\%$
Readout fidelity ($\|e\rangle$)	$F_{e\mathcal{E}} = 95.3 \pm 0.5\,\%$

TABLE S1. **Device parameters**. Measured qubit, storage, and readout cavity parameters. These independently measured values are necessary to determine for the transition and emission matrices. This enables the hidden Markov model to capture the behavior of the system during the measurement sequence.

Detector efficiency

The detector efficiency and false positive probability is determined at varying thresholds for detection λ_{thresh}. As the detection threshold is increased, more parity measurements are required to determine the presence of a photon. This suppresses false positives due to qubit errors but also leads to a decrease in the detector efficiency as events with low likelihood ratio are now rejected (Fig. S7). For large thresholds where $\frac{1}{\lambda_{\text{thresh}}+1} < \delta$, the qubit based errors are no longer the dominant source of detector errors. These errors occur due to the presence of a background of real photons whose population is given by the efficiency corrected false positive probability δ/η (shown in the main text).

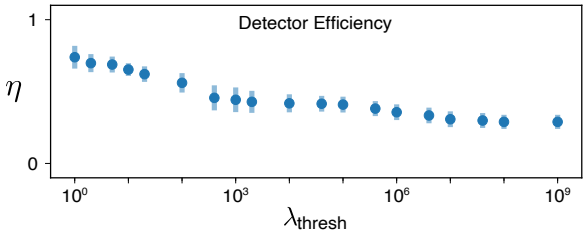

FIG. S7. **Detector efficiency as a function of detection threshold.** As the threshold for detection become stricter, the detector efficiency decreases. The efficiency scales linearly with the threshold, while the the false positive probability due to the detector errors decreases exponentially.

Analysis with cavity backgrounds

In the initial application of the hidden Markov analysis, the cavity background population is set to zero to exclude the effects of cavity heating events during the measurement. We measure a background population of $7.3 \pm 2.9 \times 10^{-4}$ and then include $\bar{n}_c$ in the model to reanalyze the data. Now in addition to the possibility of a photon from injection or background initially occupying the cavity, we allow for both cavity heating during the measurement and qubit errors. The reconstructed false positive probability of the detector $P(n = 0)$ is set by the

probability of a cavity heating event preceding the first parity measurement $\bar{n}_c \times (1 - e^{-t_m/T_1^s}) = 1.3 \times 10^{-5}$. Therefore, the maximum likelihood ratio of the reconstructed probabilities cannot exceed the cavity heating limit. By setting the detection threshold to $\lambda_{\text{thresh}} = 2.0 \times 10^4$ and including cavity heating processes in the model, we measure the background population of the cavity to be $5.6 \pm 1.8 \times 10^{-4}$, which is consistent with the initial measurement of $\bar{n}_c = 7.3 \pm 2.9 \times 10^{-4}$. This reinforces our belief that repeated parity measurements successfully mitigate qubit based errors and that cavity background photons are the limiting process for photon detection.

Sources of cavity backgrounds

The measured photon background contains a contribution from spurious photons injected due to the cavity interaction with the qubit. To characterize the significance of the effect of converted qubit excitations, we recognize that cavity ($|\tilde{1}\rangle$) and qubit ($|\tilde{e}\rangle$) excitations are dressed due to their interaction. In the dispersive limit, written in terms of the bare basis eigenstates ($|e\rangle, |1\rangle$), the dressed states are:

$$\begin{aligned} |\tilde{e}\rangle &= \sin\theta\,|g,1\rangle + \cos\theta\,|e,0\rangle \\ |\tilde{1}\rangle &= \cos\theta\,|g,1\rangle - \sin\theta\,|e,0\rangle \end{aligned} \tag{S1}$$

where θ is the mixing angle between the two systems. Qubit heating events from quasiparticle tunneling, in effect, prepare the system in the state $|e,0\rangle = |\tilde{e}\rangle - \frac{\sin\theta}{\cos\theta}|\tilde{1}\rangle$. The probability that the heating event manifests as a cavity excitation is $(\frac{\sin\theta}{\cos\theta})^2 = 3.5 \times 10^{-3}$. Therefore, the contribution of qubit heating events converted to cavity photons is determined by the probability that there is a qubit heating event and the probability that it is projected into a cavity excitation, $\bar{n}_c^q = \bar{n}_q \times (\frac{\sin\theta}{\cos\theta})^2 = 1.8 \pm 0.1 \times 10^{-4}$.

Converting cavity occupation limit to hidden photon exclusion

Kinetic mixing angle exclusion

For a dark matter candidate on resonance with the cavity frequency ($m_{\text{DM}}c^2 = \hbar\omega_c$), the rate of photons deposited in the cavity by the coherent build up of electric field in one cavity coherence time is given by [9]:

$$\frac{dN_{\text{HP}}}{dt} = \frac{U/\omega_s}{T_1^s} = \frac{1}{2}\frac{E^2 V}{\omega_s}\frac{\omega_s}{Q_s} = \frac{1}{2}\frac{J_{\text{DM}}^2 Q_{\text{DM}}^2}{m^2}\frac{Q_s}{Q_{\text{DM}}} GV \frac{1}{Q_s} \tag{S2}$$

The cavity coherence time is given by $T_1^s = \frac{Q_s}{\omega_s}$. The volume of the cavity is $0.953 \times 3.48 \times 3.56\,\text{cm}^3 = 11.8\,\text{cm}^3$. $\mathcal{G}$ encompasses the total geometric factor of the particular cavity used in the experiment. This includes a factor of 1/3 due to the dark matter field polarization being randomly oriented every coherence time. For the lowest order mode of the rectangular cavity coupled to the qubit with $\mathbf{E} = \sin(\frac{\pi x}{l})\sin(\frac{\pi y}{w})\mathbf{z}$ the geometric form factor is given by:

$$G = \frac{1}{3}\frac{\left|\int dV E_z\right|^2}{V\int dV\,|E_z|^2} = \frac{1}{3}\frac{2^6}{\pi^4} \tag{S3}$$

Since the cavity decay and dephasing times (T_1^s and T_2^s) are longer than the dark matter coherence ($Q_{\text{DM}} = 10^6$), the cavity is displaced $\frac{Q_s}{Q_{\text{DM}}}$ times with a random phase each dark matter coherence time. The cavity field displacement follows a random walk, leading to an signal amplitude enhancement by a factor of $\sqrt{\frac{Q_s}{Q_{\text{DM}}}}$.

The hidden photon generated current is set by the density of dark matter in the galaxy $\rho_{\text{DM}} = 0.4\,\text{GeV/cm}^3 = 2\pi \times 9.67 \times 10^{19}\,\text{GHz/cm}^3$:

$$J_{\text{DM}}^2 = 2\epsilon^2 m^4 A'^2 = 2\epsilon^2 m^2 \rho_{\text{DM}} \tag{S4}$$

Substituting Eqn. S4 into Eqn. S2 yields the signal rate of photons deposited in the cavity by a hidden photon dark matter candidate:

$$\frac{dN_{\text{HP}}}{dt} = \epsilon^2 \rho_{\text{DM}} Q_{\text{DM}} GV \tag{S5}$$

The total number of photons we expect to be deposited is determined by the photon rate and the integration time ($T_1^s \times N_{\text{meas}} = 8.33\,\text{s}$):

$$N_{\text{HP}} = \frac{dN_{\text{HP}}}{dt} \times T_1^s \times N_{\text{meas}} = \frac{\epsilon^2 \rho_{\text{DM}} Q_{\text{DM}} Q_s GV N_{\text{meas}}}{\omega_s} \tag{S6}$$

Calculating 90% confidence limit

By counting single photons when the applied drive population less than the background population ($\bar{n}_c$) we perform a hidden photon search. We count $N = 9$ background photons in $N_{\text{meas}} = 15{,}141$ measurements. We determine the hidden photon mixing angle ϵ that can be excluded at the 90% confidence level by computing the probability that the signal could result in less than or equal to 9 photons measured ($N \leq 9$) with less than 10% probability. In each measurement a photon is counted or not so the signal is described by a binomial distribution with probability set by the expected number of deposited photons as calculated in Eqn. S6. The systematic uncertainties of the various experimentally determined quantities in Eqn. S6 are treated as nuisance

Expt. Parameter	Θ	σ_Θ
Quantum efficiency	$\eta = 0.409$	$\sigma_\eta = 0.055$
Storage cavity frequency	$\omega_s = 6.011\,\mathrm{GHz}$	$\sigma_{\omega_s} = 205\,\mathrm{Hz}$
Storage quality factor	$Q_s = 2.06 \times 10^7$	$\sigma_{Q_s} = 8.69 \times 10^5$
Storage cavity volume	$V = 11.8\,\mathrm{cm}^3$	$\sigma_V = 0.2\,\mathrm{cm}^3$
Storage form factor	$G = 0.22$	$\sigma_G = 0.003$

TABLE S2. **Experimental parameters**. Systematic uncertainties of physical parameters in the experiment must be incorporated in determining the excluded hidden photon mixing angle ϵ. The uncertainty in the quantum efficiency is determined in the main text from fitting the relation between the measured and injected photon population at a detection threshold of $\lambda_{\mathrm{thresh}} = 10^5$. The storage cavity frequency uncertainty is obtained by Ramsey interferometry. The quality factor of the cavity is given by $Q_s = \omega_s T_1^s$ so the uncertainty is calculated as $\sigma_{Q_s}^2 = (\omega_s \sigma_{T_1^s})^2 + (T_1^s \sigma_{\omega_s})^2$. The volume uncertainty is estimated by assuming machining tolerances of 0.005 inches in each dimension. The form a factor uncertainty is estimated from assuming 1% error in the simulated structure. Of the experimental quantities, the efficiency has largest fractional uncertainty (13%), though the statistical fluctuations of the observed counts still dominate (33%).

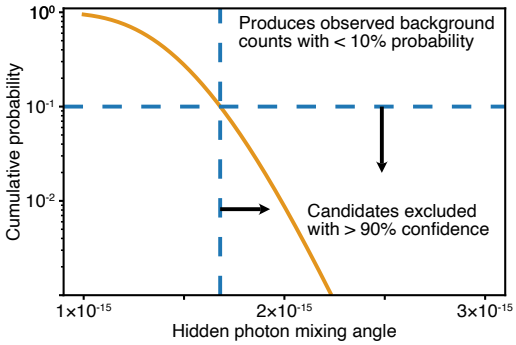

FIG. S8. **Cumulative probability of hidden photon candidate producing observed signal.** Regions where the cumulative probability falls below 0.1 are ruled out as potential hidden photon candidates with 90% confidence. The minimum mixing angle that can be excluded with 90% confidence is 1.68×10^{-15}.

parameters [10] with an assumed Gaussian distribution of mean Θ and standard deviation σ_Θ as shown in Table S2. We marginalize over the nuisance parameters [11] and compute the cumulative probability shown in Eqn. S7.

$$P(\leq N) = \int_0^\infty \prod_i d\Theta_i' \frac{e^{-(\Theta_i - \Theta_i')^2/2\sigma_{\Theta_i}^2}}{\sqrt{2\pi}\sigma_{\Theta_i}} \sum_{k=0}^{N} \frac{N_{\mathrm{meas}}!}{k!(N_{\mathrm{meas}}-k)!} \times \left(\frac{\eta' \epsilon^2 \rho_{\mathrm{DM}} Q_{\mathrm{DM}} Q_s' G' V'}{\omega_s'}\right)^k \times \left(1 - \frac{\eta' \epsilon^2 \rho_{\mathrm{DM}} Q_{\mathrm{DM}} Q_s' G' V'}{\omega_s'}\right)^{N_{\mathrm{meas}}-k} \tag{S7}$$

For a given hidden photon candidate, a cumulative probability of < 0.1 implies that candidate has less than 10% chance of producing the observed signal, thereby excluding such a candidate with 90% confidence. This leads us to exclude, with 90% confidence, hidden photon candidates with $\epsilon^{90\%} > 1.68 \times 10^{-15}$ as seen in Fig. S8

Hidden photon parameter space exclusion

Single photon counting with repeated parity measurements is sensitive to a wide range of candidates in the parameter space of hidden photon mass ($m_{\gamma'}$) and kinetic mixing angle (ϵ). To determine the sensitivity of the detector to a particular candidate, there are two considerations: the photon number dependent shift of the qubit transition as a function of the hidden photon mass, and the probability that a candidate would result in the measurement of a photon with probability larger than excluded. The photon population excluded as the 90% confidence level is computed using the excluded mixing angle $\epsilon^{90\%}$ and Eqn. S6 as $\bar{n}_{\mathrm{HP}}^{90\%} = \frac{N_{\mathrm{HP}}^{90\%}}{N_{\mathrm{meas}}} = 2.42 \times 10^{-3}$.

The photon dependent shift of the qubit transition as a function of the frequency of an external drive is determined in Gambetta et. al. [12] to be $2\chi + \omega_c - \omega_{\gamma'}$ where $\hbar\omega_{\gamma'} = m_{\gamma'}c^2$. The efficiency of an individual parity measurement for a photon dependent shift that is incommensurate with the nominal shift 2χ is given by $\eta_{\mathrm{parity}} = |\frac{1}{2}(e^{i\pi(2\chi+\omega_c-\omega_{\gamma'})/2\chi} - 1)|^2$ (Fig. S9). The effect of an inefficient parity measurement is modeled as a higher probability of qubit error in the hidden Markov model. The data is then reanalyzed and the efficiency of detection in the presence of the additional error is extracted (Fig. S9).

We note that for large detunings of the external drive, the shifted qubit transition frequency is out of the band of the $\pi/2$ pulses used in the parity measurement. The pulse shapes are Gaussian with $\sigma = 6\,\mathrm{ns}$. This constrains the maximum addressable dark matter detuning from the cavity.

A hidden photon candidate that could result in more detector counts than background counts is only possible if the population of the odd number states of the cavity state (P_{odd}) induced by the hidden photon is larger than the excluded hidden photon probability ($\bar{n}_{\mathrm{HP}}^{90\%}$). To calculate this P_{odd} we again follow Gambetta et. al. [12].

$$P_{\mathrm{odd}} = \frac{1}{\pi} \sum_{k=0}^{\infty} \mathrm{Re}\left(\frac{\frac{1}{(2k+1)!}(-A)^{2k+1} e^A}{2(2\pi/T_2^{q,\mathrm{echo}} + \Gamma_m) + (2k+1)2\pi/T_1^c}\right) \tag{S8}$$

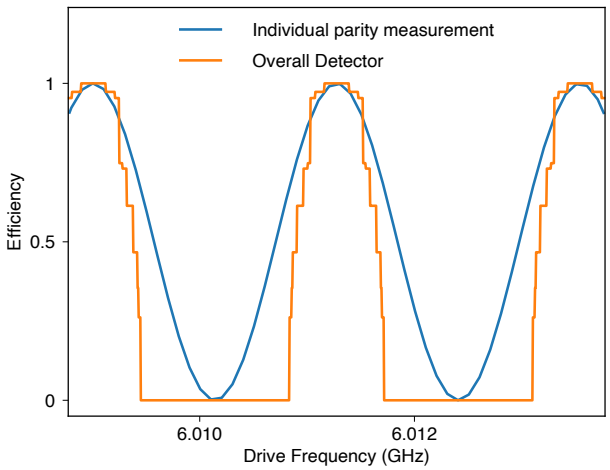

FIG. S9. **Parity measurement and detector efficiency.** The efficiency of an individual parity measurement (blue) is sinusoidal in the frequency of the hidden photon induced drive $\omega_{\gamma'}$. The detector is a series of 30 repeated parity measurements and operates with an efficiency shown in orange.

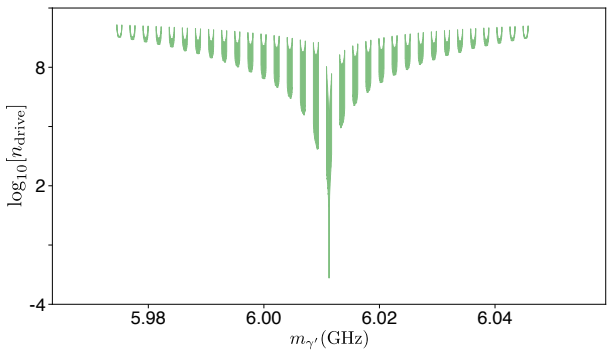

FIG. S10. **Excluded $n_{\rm drive}$ as a function of $\omega_{\gamma'}$.** The shaded region indicates $n_{\rm drive}$ induced by the hidden photon that result in $P_{\rm odd} \geq \bar{n}_{\rm HP}^{90\%}$ that are detectable and are therefore excluded as possible candidates.

where $A = D\frac{\pi/T_1^c - i\chi - i(\omega_c - \omega_{\gamma'})}{\pi/T_1^c + i\chi + i(\omega_c - \omega_{\gamma'})}$ and $\Gamma_m = D\frac{\pi}{T_1^c}$ with the distinguishability $D = \frac{2(n_- + n_+)\chi^2}{(\pi/T_1^c)^2 + \chi^2 + (\omega_c - \omega_{\gamma'})^2}$. n_- and n_+ are related to the drive strength ($n_{\rm drive}$) in units of photons: $n_\pm = \frac{n_{\rm drive}(\pi/T_1^c)^2}{(\pi/T_1^c)^2 + (\omega_c - \omega_{\gamma'} \pm \chi)^2}$. At a given hidden photon mass, we calculate all $n_{\rm drive}$ such that $P_{\rm odd} \geq \bar{n}_{\rm HP}^{90\%}$.

We note that for external drives with large amplitudes, the shifted qubit transition frequency will be out of the band of the $\sigma = 6\,$ns Gaussian $\pi/2$ pulses used in the parity measurement. This constrains the maximum addressable dark matter induced photon occupation.

By combining the detector efficiency with the $n_{\rm drive}$ such that $P_{\rm odd} \geq \bar{n}_{\rm HP}^{90\%}$, we determine all $n_{\rm drive}$ to which the repeated parity measurements are sensitive enough to detect and exclude (Fig. S10). Using Eqn. S6 we convert the excluded $n_{\rm drive}$ to a region of excluded hidden photon mixing angle (ϵ).

The above calculations assume an infinitely narrow dark matter line. To obtain the excluded region of the hidden photon kinetic mixing angle, we must account for the lineshape of the dark matter [13]. We convolve the dark matter lineshape, characterized by $Q_{\rm DM} \sim 10^6$, with the region shown in Fig. S10 to obtain the excluded ϵ shown in the main text.

We note that the storage cavity contains an infinite set of discrete resonances each with a unique coupling to the dark matter. We focus only on the lowest order mode that is specifically designed to couple to the qubit. In principle, the interactions between any modes and the dark matter could result in additional sensitivity to the hidden photon. This would require the mode of interest to have a sufficiently large geometric form factor as well as a resolvable photon number dependent qubit shift. Future dark matter searches could employ structures with multiple resonances to enable multiple simultaneous searches.

Future dark matter search

In order to implement a full scale axion search, the photon counting device must be coupled to a microwave cavity bathed in a magnetic field that accumulates the axion deposited signal. To extract the signal, a nonlinear element such as a Josephson parametric converter can be used to transfer the signal photon from the accumulation cavity to the storage cavity [14, 15]. When the accumulation cavity frequency is tuned to search for a different axion mass, the converter can be pumped at appropriate frequency to enable photon transfer. The storage cavity and qubit can remain fixed in frequency, which leaves the photon detection protocol unchanged at each tuning. Although novel cavity techniques to achieve high Q in the presence of magnetic fields have been demonstrated [16], in the most pessimistic scenario the accumulation cavity will be made of copper and limited to a $Q \sim 10^4$ at 10 GHz due to the anomalous skin effect. This sets the accumulation time to $\sim 1\,\mu$s. To minimize the dead time of the experiment, the time required to measure the storage cavity should ideally be matched to that of a copper accumulation cavity lifetime. Reaching the required detector error probability in this limited time will be challenging. In this work, each parity measurement requires 10 µs because of the large readout signal necessary to overcome the HEMT amplifier noise. We perform 30 repeated measurements in order to reduce the probability of detector errors to a level below the expected signal photon probability for dark matter ($\bar{n}_{\rm axion} \sim 10^{-8}$). Readout of a superconducting qubit with $> 99\%$ fidelity in 100 ns has been achieved by using quantum limited

parametric amplifiers [17] and appropriate pulse shaping [18]. Both techniques can be applied to this protocol to significantly increase the measurement rate and readout fidelity.

For a hidden photon search, a magnetic field is not required. As demonstrated in this work, the accumulation and storage cavity can be the same device. When the cavity is tuned to search through the parameter space, as long as a sufficiently large dispersive shift to the accumulation/storage is maintained and the qubit is still far detuned, the fundamental QND interaction between the qubit and photon is maintained. Additionally, by using extremely high Q cavities ($Q \gg Q_{\mathrm{DM}}$) to sample the dark matter energy distribution once or twice per dark matter linewidth, only $Q_{\mathrm{DM}} \sim 10^6$ cavity frequency tunings are required to test each mass hypothesis in a frequency octave.

* avdixit@uchicago.edu

[1] C. U. Lei, L. Krayzman, S. Ganjam, L. Frunzio, and R. J. Schoelkopf, Applied Physics Letters **116**, 154002 (2020).

[2] V. Ambegaokar and A. Baratoff, Phys. Rev. Lett. **10**, 486 (1963).

[3] J.-H. Yeh, J. LeFebvre, S. Premaratne, F. C. Wellstood, and B. S. Palmer, Journal of Applied Physics **121**, 224501 (2017).

[4] M. Pechal, L. Huthmacher, C. Eichler, S. Zeytinolu, A. Abdumalikov, S. Berger, A. Wallraff, and S. Filipp, Phys. Rev. X **4** (2014), 10.1103/physrevx.4.041010.

[5] P. Kurpiers, P. Magnard, T. Walter, B. Royer, M. Pechal, J. Heinsoo, Y. Salath, A. Akin, S. Storz, J.-C. Besse, and et al., Nature **558**, 264267 (2018).

[6] S. Rosenblum, Y. Y. Gao, P. Reinhold, C. Wang, C. J. Axline, L. Frunzio, S. M. Girvin, L. Jiang, M. Mirrahimi, M. H. Devoret, and et al., Nature Communications **9** (2018), 10.1038/s41467-018-03059-5.

[7] P. Magnard, P. Kurpiers, B. Royer, T. Walter, J.-C. Besse, S. Gasparinetti, M. Pechal, J. Heinsoo, S. Storz, A. Blais, and et al., Phys. Rev. Lett. **121** (2018), 10.1103/physrevlett.121.060502.

[8] X. Jin, A. Kamal, A. Sears, T. Gudmundsen, D. Hover, J. Miloshi, R. Slattery, F. Yan, J. Yoder, T. Orlando, and et al., Phys. Rev. Lett. **114** (2015), 10.1103/physrevlett.114.240501.

[9] S. Chaudhuri, P. W. Graham, K. Irwin, J. Mardon, S. Rajendran, and Y. Zhao, Phys. Rev. D **92** (2015), 10.1103/physrevd.92.075012.

[10] W. A. Rolke, A. M. Lpez, and J. Conrad, Nuclear Instruments and Methods in Physics Research Section A: Accelerators, Spectrometers, Detectors and Associated Equipment **551**, 493503 (2005).

[11] J. Conrad, O. Botner, A. Hallgren, and C. Prez de los Heros, Physical Review D **67** (2003), 10.1103/physrevd.67.012002.

[12] J. Gambetta, A. Blais, D. I. Schuster, A. Wallraff, L. Frunzio, J. Majer, M. H. Devoret, S. M. Girvin, and R. J. Schoelkopf, Phys. Rev. A **74**, 042318 (2006).

[13] J. W. Foster, N. L. Rodd, and B. R. Safdi, Phys. Rev. D **97** (2018), 10.1103/physrevd.97.123006.

[14] C. J. Axline, L. D. Burkhart, W. Pfaff, M. Zhang, K. Chou, P. Campagne-Ibarcq, P. Reinhold, L. Frunzio, S. M. Girvin, L. Jiang, *et al.*, Nature Physics **14**, 705710 (2018).

[15] N. Leung, Y. Lu, S. Chakram, R. Naik, N. Earnest, R. Ma, K. Jacobs, A. Cleland, and D. Schuster, npj Quantum Information **5** (2018).

[16] D. Alesini, C. Braggio, G. Carugno, N. Crescini, D. D'Agostino, D. D. Gioacchino, R. D. Vora, P. Falferi, U. Gambardella, C. Gatti, *et al.*, "High quality factor photonic cavity for dark matter axion searches," (2020), preprint at https://arxiv.org/abs/2002.01816.

[17] T. Walter, P. Kurpiers, S. Gasparinetti, P. Magnard, A. Potonik, Y. Salath, M. Pechal, M. Mondal, M. Oppliger, C. Eichler, *et al.*, Phys. Rev. Appl. **7** (2017).

[18] D. McClure, H. Paik, L. Bishop, M. Steffen, J. M. Chow, and J. M. Gambetta, Phys. Rev. Appl. **5** (2016).